

# Size affected dislocation activity in crystals: Advanced surface and grain boundary conditions



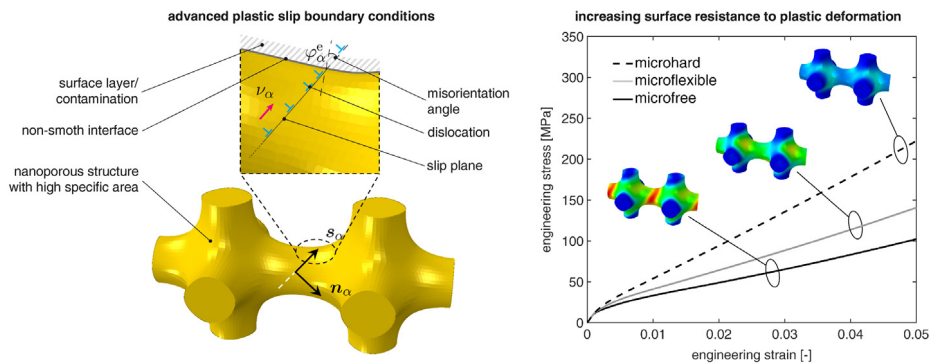
Edgar Husser<sup>a,b,\*</sup>, Celal Soyarslan<sup>c</sup>, Swantje Bargmann<sup>c</sup>

<sup>a</sup> Institute of Continuum Mechanics and Material Mechanics, Hamburg University of Technology, Germany

<sup>b</sup> Institute of Materials Research, Materials Mechanics, Helmholtz-Zentrum Geesthacht, Germany

<sup>c</sup> Chair of Solid Mechanics, School of Mechanical Engineering and Safety Engineering, University of Wuppertal, Germany

## GRAPHICAL ABSTRACT



## ARTICLE INFO

### Article history:

Received 14 October 2016

Received in revised form

20 December 2016

Accepted 19 January 2017

Available online 23 January 2017

### Keywords:

Higher-order boundary conditions  
Gradient extended crystal plasticity  
Defect density  
Size effect  
Surface yielding  
Nanoporous gold

## ABSTRACT

Extended crystal plasticity theories are well established to study size-dependent hardening of metals. Surface and inner grain boundary conditions play a significant role for crystals at small scales as they affect the dislocation activity and, hence, alter strength and strain hardening behavior. Conventional micro boundary conditions, i.e., microhard and microfree, are unable to capture the underlying physics as they describe ideal and over-simplified surface/interface conditions. In this work, advanced boundary conditions for gradient extended crystal plasticity are introduced to map realistic conditions at external surfaces, interphases, or grain boundaries. They relate the magnitude of plastic slip to surface defect density and slip directions with respect to the surface normal. Characteristic features are highlighted, including the effect of surface yielding and size dependent surface strengthening.

© 2017 The Authors. Published by Elsevier Ltd.

This is an open access article under the CC BY-NC-ND license (<http://creativecommons.org/licenses/by-nc-nd/4.0/>).

## 1. Introduction

In crystalline solids, perfect crystalline behavior ceases to exist near external surfaces, grain boundaries between two crystals of

the same phase and interphase boundaries between two different phases [1,2]. Since the binding of an atom to its neighbors contributes a negative term to the energy of a crystal, Gibbs free energy at these surfaces is modified due to inhomogeneities at the nanoscale, such as altered bonds. This difference in bonding as compared to the bulk generally causes an extra surface stress [3]. Dislocation dynamics and, thus, macroscopic plastic behavior is also influenced by the presence of a surface to create size effects on

\* Corresponding author at: Institute of Continuum Mechanics and Material Mechanics, Hamburg University of Technology, Germany.

E-mail address: [edgar.husser@tuhh.de](mailto:edgar.husser@tuhh.de) (E. Husser).

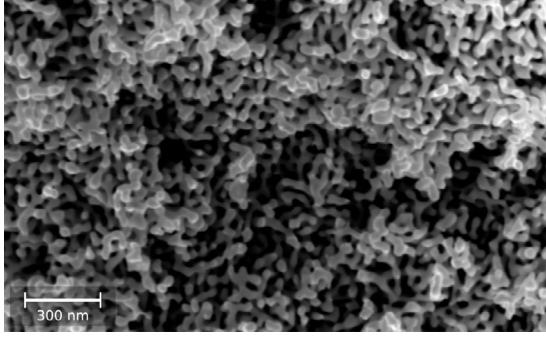


**Fig. 1.** Scanning electron micrograph of nanoporous gold with an exceptionally high surface-to-volume ratio.

Source: Reprinted from [7].

© 2016, With permission from Elsevier. (Image courtesy of Nadiia Mameka at Helmholtz-Zentrum Geesthacht.)

yield stress and work hardening. The surface's influence becomes substantial once the number of atoms sitting at the surface relative to those lying within the bulk increases, e.g., in the case of ultra-fine-grained metals, thin films, nanoporous materials [4].

With its nanoscale porosity and high specific surface area, nanoporous gold demonstrates extreme chemo-mechanical activity [5]. Its catalytic activity, electrical conductivity, morphological properties (e.g., high specific surface area), and mechanical properties (e.g., reduced stiffness), make nanoporous gold attractive in numerous applications such as actuation, catalysis, sensors and microfluids [5–7]. In nanoporous gold the load bearing structure is a network of ligaments (cf. Fig. 1) with diameters of 5 nm to several micrometers, depending on the post annealing treatment [8–10]. Although brittle in tension, nanoporous gold shows considerable malleability, that is, extreme ductility under compressive stress in the vicinity of crack tips with ligaments occasionally strained by as much as 200% [11,12]. Microscopic characterization of fracture surfaces indicated that dislocation activity is suppressed in nanoscale ligament structures while dislocation activity is present in heat treated nanoporous gold with average ligament diameter of  $\approx 1 \mu\text{m}$  [11]. In addition to the effect of suppressed dislocation nucleation [13], emission and reabsorption of dislocations at free surfaces is another source of size dependent hardening [14].

In this work, we study the plastic<sup>1</sup> deformation behavior of nanoporous gold in the context of gradient extended crystal plasticity at finite strains. The focus is on novel higher-order boundary conditions reflecting microscopically non-idealized conditions at external surfaces, grain boundaries, or interfaces. In the vast majority of analytical and numerical studies, two types of simple, idealized boundary conditions are adopted, namely microfree and microhard. The former characterizes conditions with vanishing micro-stresses, i.e., no microscopic force conjugated to geometrically necessary dislocations (GNDs) occurs as a driving force on the body. Dislocations are free to escape at the surface, hence no dislocation pile-ups occur. At the other extreme, i.e., for microhard conditions, plastic slip vanishes at the boundary, preventing any dislocation escape.

Non-idealized boundary conditions are of interest, for instance, if the exterior causes additional resistance to plastic deformation or, in other words, if dislocations are not enabled to move unrestricted through the surface. Related discussions, including size effects on the yield stress and work hardening as well as the impact of surface effects on fracture properties, are found in [16].

<sup>1</sup> The influence of surfaces on the elastic behavior is studied in another work; elastic and plastic Poisson's ratios of nanoporous gold were investigated experimentally and numerically in [15].

Oxidation on nanoporous gold films<sup>2</sup> is higher than on planar gold due to increased catalytic activity of the porous network [20,21]. Buckley [17] demonstrated that thin films on the surface of single crystal Au increased the surface hardness. This was attributed to increased resistance to plastic deformation by the impeded escape of dislocations by the presence of the oxide film, referred to as the Roscoe effect [22].<sup>3</sup> Therefore, mechanical properties of small-scaled samples are related (to some extent) to their surfaces.

Although highly relevant, this aspect of dislocation-surface interaction modeling has not been studied in the literature for nanoporous gold. With this work, we attempt to bridge this gap by presenting computational modeling of advanced higher-order boundary conditions for Au single crystals. As a demonstrative example, their impact on the deformation response of a periodic nanoporous Au microstructure is examined. The chosen geometry is characterized by a typical microstructural feature with curved surfaces frequently found in nanoporous metals. This results in many diverse misorientation angles.

Grain boundary conditions, i.e., inner boundaries in polycrystals, which are physically more meaningful than their idealized counterparts have been studied by [24–29]. Only very few works are devoted to a computational framework for surface effects in single crystals. In these, the formation of surface steps during plastic deformation is taken as an additional source for size-dependent hardening and strengthening [30,31]. The conditions proposed in this work are more general and capable of modeling a wide range of dislocation-surface interactions.

## 2. Gradient extended single crystal plasticity

### 2.1. Basic relations

The thermodynamic consistent framework for gradient-enhanced crystal plasticity is recalled based on [32]. The large deformation theory is employed in terms of the multiplicative decomposition of the deformation gradient  $\mathbf{F} = \mathbf{F}_E \cdot \mathbf{F}_P$ , where  $\mathbf{F}_E$  is the pure elastic and  $\mathbf{F}_P$  the plastic deformation part. As usual, this motivates the right Cauchy–Green stretch tensors  $\mathbf{C} = \mathbf{F}^T \cdot \mathbf{F}$  and  $\mathbf{C}_E = \mathbf{F}_E^T \cdot \mathbf{F}_E$ . Furthermore, the first and second Piola–Kirchhoff stress denoted as  $\mathbf{P}$  and  $\mathbf{S}_E$ , respectively, are of interest. The relation between these stress measures is given by  $\mathbf{P} = \mathbf{F}_E \cdot \mathbf{S}_E \cdot \mathbf{F}_P^{-T}$ . For the particular choice of a Neo-Hookean hyperelastic material behavior, the second Piola–Kirchhoff stress yields

$$\mathbf{S}_E = \mu \mathbf{I} + [\lambda \ln(J) - \mu] \mathbf{C}_E^{-1}, \quad (1)$$

where  $J = \det(\mathbf{F}_E)$  is the Jacobian determinant;  $\mu$  and  $\lambda$  denote the Lamé parameters. Moreover, the Mandel stress is introduced as  $\mathbf{M}_E = \mathbf{C}_E \cdot \mathbf{S}_E$  – the work conjugate to the plastic velocity gradient  $\mathbf{L}_P = \dot{\mathbf{F}}_P \cdot \mathbf{F}_P^{-1} = \sum_{\alpha} v_{\alpha} [\mathbf{s}_{\alpha} \otimes \mathbf{n}_{\alpha}]$  which is defined via plastic slip rates  $v_{\alpha}$  on corresponding slip planes  $\mathbf{s}_{\alpha} \otimes \mathbf{n}_{\alpha}$ . In this respect, the crystallographic geometry of each slip system  $\alpha$  is specified in terms of slip direction  $\mathbf{s}_{\alpha}$ , slip plane normal  $\mathbf{n}_{\alpha}$ , and transverse slip direction  $\mathbf{t}_{\alpha} = \mathbf{n}_{\alpha} \times \mathbf{s}_{\alpha}$ . It is further assumed that plastic deformation is lattice preserving.

<sup>2</sup> At temperatures less than 900 °C gold does normally not form a stable oxide in air or oxygen [17,18]. However, electrochemical techniques allow generation of oxides on gold surface [19].

<sup>3</sup> This scenario is not limited to gold. It is demonstrated in [23] that, on the course of deformation the oxide films in aluminum causes formation of a layer of edge dislocation dipoles trapped beneath the surface and reduction of the amount of surface slip. This reduction is observed to be larger for the increased oxide coating thickness. Hence, the proposed methodologies in this work have a wide range of applications although the current application is concentrated on the nanoporous gold.

The mathematical model is formulated in consistency with the second law of thermodynamics. Omitting a detailed derivation for the sake of brevity, the reduced dissipation inequality reads

$$\mathcal{D}_{\text{red}} = \sum_{\alpha} \left[ \int_{\mathcal{B}_i} \nu_{\alpha} [\tau_{\alpha} + \text{Div}_i(\kappa_{\alpha})] dV_i + \int_{\partial \mathcal{B}_i} \nu_{\alpha} \kappa_{\alpha} \cdot \mathbf{N}_i^{(b)} dA_i \right] \geq 0, \quad (2)$$

where  $\tau_{\alpha} = \mathbf{s}_{\alpha} \cdot \mathbf{M}_E \cdot \mathbf{n}_{\alpha}$  is the stress resolved on slip system  $\alpha$ ,  $\text{Div}_i(\kappa_{\alpha})$  represents the backstress associated with GND storage, and  $\mathbf{N}_i^{(b)}$  denotes the outward pointing normal vector of the intermediate area element  $dA_i$ . Finally, a micro hardening stress<sup>4</sup>  $\kappa_{\alpha}$  of backstress character is introduced

$$\kappa_{\alpha} = -l_{\alpha}^2 |\mathbf{b}_{\alpha}| \left[ H_0^e \mathbf{s}_{\alpha} \int_{t_0}^t \dot{g}_{i\alpha}^e dt + H_0^s \mathbf{t}_{\alpha} \int_{t_0}^t \dot{g}_{i\alpha}^s dt \right]. \quad (3)$$

Here,  $g_{i\alpha}^e$  and  $g_{i\alpha}^s$  denote the geometrically necessary edge and screw dislocation densities,  $\mathbf{b}_{\alpha}$  is the Burgers vector, and  $H_0^e$  is the gradient hardening modulus with respect to edge GND components. Hardening associated with screw GND components is taken as  $H_0^s = [1 - \nu]H_0^e$ , according to their elastic strain energy ratio, where  $\nu$  is the Poisson's ratio. Finally,  $l_{\alpha}$  is the internal length scale.

## 2.2. Governing equations

The evolution of edge and screw GND densities is governed by

$$\dot{g}_{i\alpha}^e = -|\mathbf{b}_{\alpha}|^{-1} \nabla_i \nu_{\alpha} \cdot \mathbf{s}_{\alpha} \quad \text{and} \quad \dot{g}_{i\alpha}^s = -|\mathbf{b}_{\alpha}|^{-1} \nabla_i \nu_{\alpha} \cdot \mathbf{t}_{\alpha}, \quad (4)$$

respectively. The initial GND densities are taken as zero. The sign convention assigned in Eq. (4)<sub>2</sub> defines right-handed screw dislocations to be positive. Both governing equations for GND densities are coupled to the displacement problem via stress measures. Neglecting body forces, the mechanical problem for the case of quasi-static and isothermal conditions is specified by the balance of linear momentum  $\mathbf{0} = \text{Div}_i(\mathbf{F}_E \cdot \mathbf{S}_E)$ .

The evolution of plastic slip rates is governed by a power law relation

$$\nu_{\alpha} = \nu_0 \left[ \frac{\langle \tau_{\alpha} + \text{Div}_i(\kappa_{\alpha}) \rangle}{S_{\alpha}} \right]^m, \quad \text{with } \langle \bullet \rangle = \frac{1}{2} [\bullet + |\bullet|]. \quad (5)$$

In that,  $\nu_0$  is the reference slip rate,  $m$  denotes the rate-sensitivity exponent, and

$$S_{\alpha} = Y_0 + H_0^1 \int_{t_0}^t \nu_{\alpha} dt \quad (6)$$

describes the slip system resistance associated with random trapping processes of statistically stored dislocations (SSDs) by means of the local hardening modulus  $H_0^1$ . SSDs are captured by the resulting slip in the material. Finally, the initial slip system resistance (critical resolved shear stress) is incorporated via  $Y_0$ .

## 2.3. Boundary conditions

Standard micro boundary conditions, known as microhard (on boundary  $\partial \mathcal{B}_i^{\gamma}$ ) and microfree (on boundary  $\partial \mathcal{B}_i^{\beta}$ ) [24,34], mimic idealized conditions at the crystal's surface as illustrated in Fig. 2(a) and (b). At one extreme, microhard boundaries prevent any transmission of crystallographic slip through the boundary.

In this case, the boundary deforms with maximum resistance to plastic deformation such that dislocations are compelled to pile up. This behavior is typically expressed by the condition  $\nu_{\alpha} \mathbf{N}_i^{(b)} \cdot \mathbf{s}_{\alpha} = \nu_{\alpha} \mathbf{N}_i^{(b)} \cdot \mathbf{t}_{\alpha} = 0$  on  $\partial \mathcal{B}_i^{\gamma}$ . At the other extreme, microfree boundaries prevent any dislocation pile ups along the exterior. Boundaries are transparent to dislocation motion, leading to zero resistance to plastic deformation. This situation is described by the condition  $\dot{g}_{i\alpha}^e = \dot{g}_{i\alpha}^s = 0$  on  $\partial \mathcal{B}_i^{\beta}$ .

In spirit of Ekh et al. [25], we postulate advanced microflexible boundary conditions for single crystals for which the magnitude of plastic slip at the boundary is related to the microstress:

$$\nu_{\alpha} = C_{\Gamma} l_{\alpha}^2 |\mathbf{b}_{\alpha}| H_0^e \left[ \mathbf{s}_{\alpha} \cdot \mathbf{N}_i^{(b)} \frac{\dot{g}_{i\alpha}^e}{\tan(\varphi_{\alpha}^e)} + \mathbf{t}_{\alpha} \cdot \mathbf{N}_i^{(b)} \frac{[1 - \nu] \dot{g}_{i\alpha}^s}{\tan(\varphi_{\alpha}^s)} \right] \quad (7)$$

on  $\partial \mathcal{B}_i^{\text{crystal}}$ ,

where  $C_{\Gamma} = C_{\Gamma}(g_i^{\text{eff}})$  denotes the boundary coefficient (given in unit area per energy), related to the effective GND density

$$g_i^{\text{eff}} = \sqrt{\sum_{\alpha} [g_{i\alpha}^e]^2 + [g_{i\alpha}^s]^2}. \quad (8)$$

Moreover,

$$\varphi_{\alpha}^e = \arccos \left( \left| \mathbf{s}_{\alpha} \cdot \mathbf{N}_i^{(b)} \right| \right) \quad \text{and} \quad \varphi_{\alpha}^s = \arccos \left( \left| \mathbf{t}_{\alpha} \cdot \mathbf{N}_i^{(b)} \right| \right) \quad (9)$$

are the misorientation angles measured between the boundary normal  $\mathbf{N}_i^{(b)}$  and the flow direction of the edge respectively screw dislocation, cf. the illustration in Fig. 2(c). Via Eq. (7), the slip rate on the boundary is associated with the microstress and the angle<sup>5</sup> at which dislocations escape through the boundary. Microfree and microhard boundary conditions are naturally incorporated for complete alignment and misalignment, respectively [25]. For cases in between these extremes, the proposed boundary conditions result in non-zero boundary dissipation contribution, cf. Eq. (2). With respect to  $C_{\Gamma}(g_i^{\text{eff}})$ , a natural choice might be

$$C_{\Gamma} = C_0 \exp \left( s_{\Gamma} \frac{g_i^{\text{eff}} - g^c}{g^c} \right), \quad (10)$$

in which  $C_0$  is the reference boundary coefficient,  $s_{\Gamma}$  determines the rate of dislocation absorption resp. transmission by the surface, and  $g^c$  measures dislocation pile up underneath the surface in terms of critical dislocation density and acts as a threshold for the initiation of dislocation transmission and absorption, leading to changing surface, interface resp. grain boundary conditions. For  $g_i^{\text{eff}} - g^c > 0$ ,  $C_{\Gamma}$  starts to evolve, resulting in a softening effect due to dislocation escape and absorption. This mechanism represents surface yielding as plastic deformation across the boundary increases. Furthermore, with decreasing length scales, this effect naturally becomes reinforced due to stronger interplay between dislocations and external surfaces as a result of a change in number of atoms exposed to a surface. In contrast to ideally smooth and clean grain boundaries, the proposed concept accounts for inhomogeneities at nanoscale such as surface coatings or passivation layers [35–37], damage layers induced by the FIB milling process [38–40], oxide layers [41], and may also be extended to interfacial effects in metal polymer (nano-) composites [42].

<sup>5</sup> For dislocation flow parallel to the surface area, it follows that  $1/\tan(\varphi_{\alpha}^e) \rightarrow 0$  as  $\varphi_{\alpha}^e \rightarrow \pi/2$  and, hence, the corresponding contribution within the boundary term vanishes. For dislocation flow perpendicular to the surface, a threshold is required to ensure numerical treatment of the computation of  $1/\tan(\varphi_{\alpha}^e)$  as  $\varphi_{\alpha}^e \rightarrow 0$ . Same holds for  $\varphi_{\alpha}^s$ .

<sup>4</sup> In a thermodynamic setting, the free energy acts as a potential for  $\kappa_{\alpha}$  [33].

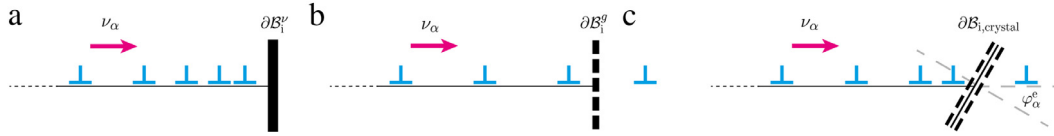


**Fig. 2.** Schematic illustration of higher-order boundary conditions: (a) microhard; (b) microfree; (c) (non-idealized) microflexible boundary conditions. While a hard boundary does not permit any slip transmission through the boundary, a free boundary is completely transparent to dislocation motion. The proposed advanced microflexible boundary conditions relate the boundary slip to the defect density and depend on the misorientation angles  $\varphi_\alpha^e$  and  $\varphi_\alpha^s$ . This allows a physically more meaningful modeling.

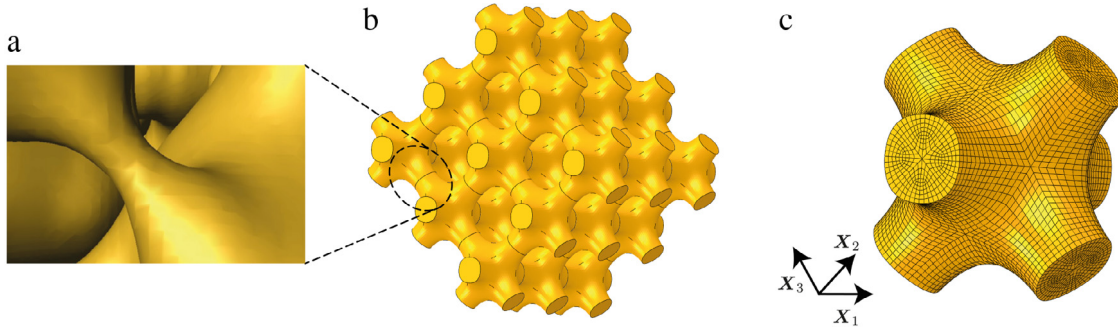


**Fig. 3.** (a) 3D FIB tomography reconstruction showing a typical structural feature in nanoporous gold with mean ligament diameter of 420 nm; (b) microstructure built up periodically by the indicated unit cell (27.5% gold volume fraction); (c) finite element mesh (25536 linear brick elements) of the periodic unit cell.

Source: Reprinted from [44].

© 2016, With permission from Elsevier.

An important aspect of higher-order boundary conditions is the treatment of the boundary term in the implementation. Due to the similarity of both GND density equations, we limit our attention to the edge component. Then, the variational form of Eq. (4) reads

$$0 = |\mathbf{b}_\alpha| \int_{\mathcal{B}_i} \delta g_\alpha^e \dot{\mathbf{s}}_\alpha^e dV_i - \int_{\mathcal{B}_i} \nu_\alpha \text{Div}_i (\delta g_\alpha^e \mathbf{s}_\alpha) dV_i + \int_{\partial \mathcal{B}_i} \delta g_\alpha^e \nu_\alpha \mathbf{N}_i^{(b)} \cdot \mathbf{s}_\alpha dA_i. \quad (11)$$

The boundary condition is then implemented via the surface term. Thus, no additional surface elements are needed.

### 3. Numerical example: nanoporous gold

We demonstrate the performance of the advanced micro boundary conditions by means of compression tests on nanoporous gold. Fig. 3(a) depicts a typical structural feature in nanoporous Au which is considered in the here investigated microstructure,<sup>6</sup> cf. Fig. 3(b). Fig. 3(c) shows the corresponding finite element mesh of the periodic unit cell consisting of 25 536 linear brick elements. The advanced boundary condition in Eq. (7) is applied to the entire surface, i.e.,  $\partial \mathcal{B}_i = \partial \mathcal{B}_{i,\text{crystal}}$ . Furthermore, periodicity is applied with respect to all displacement and GND density degrees of freedom at unit cell junctions.

Since dealloying conserves the crystal lattice of the parent alloy, the single phase ligament network does not accommodate grain boundaries [12]. Hence, the microstructure is treated as a single crystal. A single slip configuration is adopted with  $\mathbf{s}_1 = [1\bar{1}\bar{1}]/\sqrt{3}$

<sup>6</sup> To this end, the surface of the microstructure is formed as a triply periodic continuous level surface represented by an equation of the form  $h = \alpha_1 f_1 + \alpha_2 f_2 + \varpi$  [43].  $f_1 = \cos x + \cos y + \cos z$  and  $f_2 = \cos x \cos y + \cos y \cos z + \cos z \cos x$  are right-hand sides of the simple level surface approximations of the so-called  $P$  and  $W$  surfaces, respectively. The constants  $\alpha_1 = 10.0$ ,  $\alpha_2 = -5.1$ , and  $\varpi = 9.901$  supply a volume fraction of solid in the unit cell of 27.5%. The resulting periodic unit cell is scaled such that  $L_0 = \pi \mu\text{m}$  is obtained for the edge length of the cell and  $D_0 \approx 1000$  nm is obtained for the mean ligament diameter at the smallest cross-section. A second microstructure with  $L_0 = \pi/4 \mu\text{m}$ , yielding  $D_0 \approx 250$  nm, is also considered during simulations.

**Table 1**

Material parameters considered in the numerical computations.

Parameter	Symbol	Value
Young's modulus	$E$	79 GPa
Poisson's ratio	$\nu$	0.44
Burgers vector magnitude	$ \mathbf{b}_\alpha $	0.288 nm
Initial slip resistance	$Y_0$	43.47 MPa
Rate sensitivity parameter	$m$	20
Reference shear rate	$\nu_0$	$10^{-3} \text{ s}^{-1}$
Local hardening modulus	$H_0^1$	10.2 MPa
Gradient hardening modulus	$H_0^e$	150.7 MPa
Internal length scale	$l_\alpha$	1.5 $\mu\text{m}$

and  $\mathbf{n}_1 = [101]/\sqrt{2}$ , resulting in a Schmid factor of 0.4082 for compression along the [001] direction. Edge as well as screw GND densities are accounted for. The structure is loaded under displacement controlled conditions along the [001] direction up to 5% compressive strain and at a strain rate of  $10^{-3} \text{ s}^{-1}$ . The rate of dislocation absorption resp. transmission is set to  $s_r = 100$ . All material parameters for Au single crystal are listed in Table 1. The empirical approach for the determination of the initial slip resistance is adopted from Bargmann et al. [45].

First, the mechanical response of the microstructure is analyzed for  $g_i^{\text{eff}} - g^c \leq 0$  being fulfilled during the entire deformation. The results are shown in Fig. 4 for different magnitudes of  $C_0$ . The idealized response in terms of microhard and microfree boundary conditions are the upper and lower bound of the crystal's strength. For  $C_0 = 0$ , the boundary contains the highest density of defects leading to minimum plastic deformation. With increasing  $C_0$ , the ability to transmit dislocations through the boundary increases. This, in turn, leads to a softer mechanical response in terms of increasing plastic deformation. A fully transparent boundary, i.e., without any resistance to dislocation motion, is achieved in the limiting case of  $C_r \rightarrow \infty$ . This is illustrated by the contour plot inclusions on the right-hand side of Fig. 4 by means of the accumulated plastic slip distribution  $\gamma_1 = \int_{t_0}^t \nu_1 dt$ . Furthermore, a pronounced effect resulting from a reduction of the characteristic size, here from  $D_0 \approx 1000$  nm to  $D_0 \approx 250$  nm, is clearly shown for the particular case  $C_0 = 1 \mu\text{m}^2/\text{nj}$ .

Next, we study the case of an initially impenetrable interface whose resistance to plastic deformation softens after a critical dis-

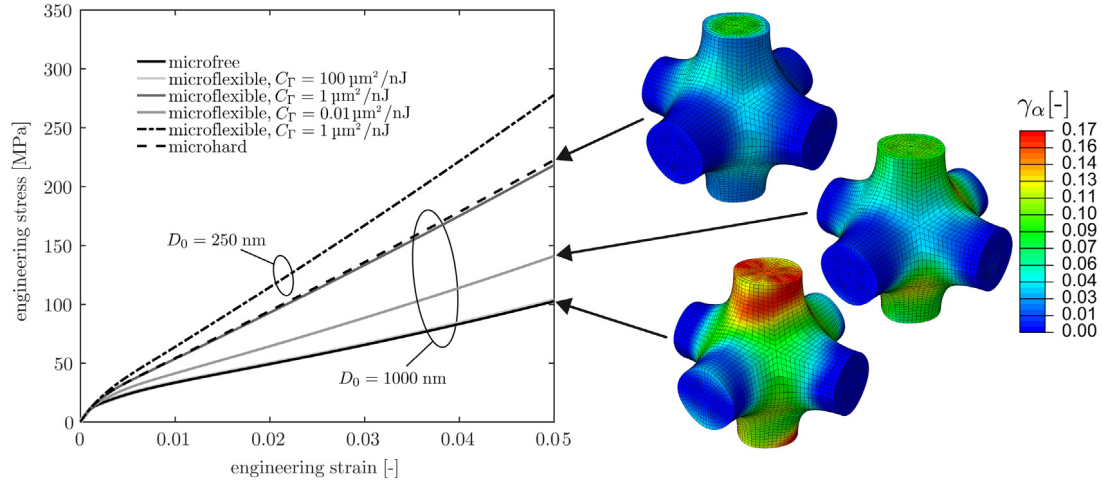


**Fig. 4.** Stress–strain response for different surface conditions illustrating the impact of the reference boundary parameter  $C_0$  if  $g^c \gg g_i^{\text{eff}}$ . The contour plots indicate the associated impact on the accumulated plastic slip distribution for both idealized cases as well as for the case of non-idealized boundary conditions. As idealized boundary conditions do not account for the impact of surface effects in a sufficient manner, they underestimate (microhard) resp. overestimate (microfree) the accumulated plastic slip.

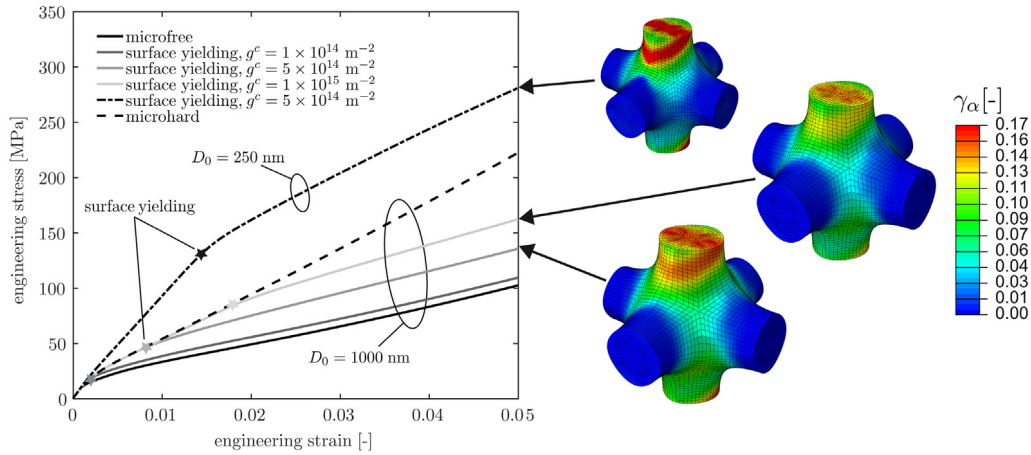


**Fig. 5.** Impact of a critical dislocation density  $g^c$  if  $C_0 = 0.01 \mu\text{m}^2/\text{nJ}$ . The star icons indicate the initiation of surface yielding associated with stage II of the boundary conditions, i.e., if  $g_i^{\text{eff}} > g^c$ . Moreover, a clear size effect is predicted for both cases if reducing the characteristic ligament size from  $D_0 = 1000 \text{ nm}$  to  $D_0 = 250 \text{ nm}$ . One can further observe an increasing surface strength with reducing ligament diameter  $D_0$ . The contour plots illustrate the impact on the localized deformation in terms of plastic slip.

location density is overcome ( $g_i^{\text{eff}} > g^c$ ). A cut-off value  $\bar{C}_R = 100 \mu\text{m}^2/\text{nJ}$  is introduced in order to ensure numerical stability of the computations during the evolution of the boundary coefficient. The impact on the mechanical response is illustrated in Fig. 5 for different threshold values  $g^c$ . As shown, dislocation-controlled surface yielding is obtained at different strain levels as a result of spontaneous initiation of plastic slip across the surface. After sufficient post deformation, the work hardening slope converges towards the stage of an almost transparent boundary. For a small ligament diameter of  $D_0 \approx 250 \text{ nm}$ , a drastic increase in surface strength and strain hardening is obtained. Here, surface yielding is initiated at a later stage of deformation in comparison to the larger microstructure. Furthermore, the inclusions on the right-hand side in Fig. 5 indicate that the characteristics of localized slip deformation – as it results for microfree conditions – decline with increasing threshold value. By reducing the size, localized plastic deformation becomes drastically intensified for the same threshold value.

The results clearly demonstrate the ability of the advanced boundary conditions to model surfaces whose properties are influenced by formation of surface films, contamination, fabrication process, coating, etc. which become non-negligible at the sub-micron scale.

#### 4. Conclusions

In extension to the microflexible boundary conditions of Ekh et al. [25] for inner grain boundaries, the advanced micro boundary conditions proposed in this contribution capture physically realistic behavior during plastic deformation compared to conventional boundary conditions. The proposed boundary conditions lead to non-zero boundary dissipation and allow to model a wide range of grain boundary behavior, including the effect of surface yielding and size dependent surface strengthening. Additional surface effects associated with the formation of surface layer, e.g., coating, passivation, oxidation, or damage, can be accounted for within the framework of gradient extended crystal plasticity. An appropriate integration procedure – without the use of additional surface elements – has been applied for a finite element implementation using linear brick elements. By means of a demonstrative problem, the impact of the non-idealized boundary conditions on the mechanical response of nanoporous Au has been illustrated. The results demonstrate characteristic features of the model. Furthermore, it has been shown that conventional microhard or microfree conditions are obtained in the limiting cases using the same numerical implementation. An application to polycrystals is straightforward.

## Acknowledgment

We gratefully acknowledge financial support from the German Research Foundation (DFG) via SFB 986 “M<sup>3</sup>”, project B6.

## References

- [1] M.P. Marder, *Condensed Matter Physics*, Wiley, Chichester, New York, 2010.
- [2] J. Martin, R. Doherty, B. Cantor, *Stability of Microstructure in Metallic Systems*, in: *Cambridge Solid State Science Series*, Cambridge University Press, 1997.
- [3] L. Sander, *Advanced Condensed Matter Physics*, Cambridge University Press, 2009.
- [4] P. van Beers, G. McShane, V. Kouznetsova, M. Geers, Grain boundary interface mechanics in strain gradient crystal plasticity, *J. Mech. Phys. Solids* 61 (12) (2013) 2659–2679.
- [5] E. Seker, M.L. Reed, M.R. Begley, Nanoporous gold: Fabrication, characterization, and applications, *Materials* 2 (4) (2009) 2188.
- [6] B.-N.D. Ngô, A. Stukowski, N. Mameka, J. Markmann, K. Albe, J. Weissmüller, Anomalous compliance and early yielding of nanoporous gold, *Acta Mater.* 93 (2015) 144–155.
- [7] J. Wilmers, A. McBride, S. Bargmann, Interface elasticity effects in polymer-filled nanoporous metals, *J. Mech. Phys. Solids* 99 (2017) 163–177.
- [8] E. Seker, J.T. Gaskins, H. Bart-Smith, J. Zhu, M.L. Reed, G. Zangari, R. Kelly, M.R. Begley, The effects of post-fabrication annealing on the mechanical properties of freestanding nanoporous gold structures, *Acta Mater.* 55 (14) (2007) 4593–4602.
- [9] M. Hakamada, M. Mabuchi, Mechanical strength of nanoporous gold fabricated by dealloying, *Scr. Mater.* 56 (11) (2007) 1003–1006.
- [10] F. Kertis, J. Snyder, L. Govada, S. Khurshid, N. Chayen, J. Erlebacher, Structure/processing relationships in the fabrication of nanoporous gold, *JOM* 62 (6) (2010) 50–56.
- [11] J. Biener, A.M. Hodge, A.V. Hamza, Microscopic failure behavior of nanoporous gold, *Appl. Phys. Lett.* 87 (12) (2005) 121908.
- [12] H.-J. Jin, L. Kurmanaeva, J. Schmauch, H. Rösner, Y. Ivanisenko, J. Weissmüller, Deforming nanoporous metal: Role of lattice coherency, *Acta Mater.* 57 (9) (2009) 2665–2672.
- [13] J.R. Greer, J.T.M. De Hosson, Plasticity in small-sized metallic systems: Intrinsic versus extrinsic size effect, *Prog. Mater. Sci.* 56 (6) (2011) 654–724.
- [14] X.Y. Sun, G.K. Xu, X.Q. Li, X. Feng, H. Gao, Mechanical properties and scaling laws of nanoporous gold, *J. Appl. Phys.* 113 (2) (2013) 023505.
- [15] L. Lühns, C. Soyarslan, J. Markmann, S. Bargmann, J. Weissmüller, Elastic and plastic Poissons ratios of nanoporous gold, *Scr. Mater.* 110 (2016) 65–69.
- [16] J.C. Grosskreutz, D.K. Benson, *The Effects of the Surface on the Mechanical Properties of Metals*, Springer US, Boston, MA, 1968, pp. 61–94.
- [17] D. Buckley, Influence of surface films on friction and deformation of single-crystal and polycrystalline gold, *Tech. rep.*, NASA TECHNICAL NOTE NASA TN D-4875, Lewis Research Center Cleveland, Ohio, 1968.
- [18] D. Clark, T. Dickinson, W.N. Mair, On the oxidation of gold, *J. Phys. Chem.* 65 (8) (1961) 1470.
- [19] G.M. Schmid, N. Hackerman, Electrical double layer capacities and adsorption of alcohols on gold, *J. Electrochem. Soc.* 110 (5) (1963) 440–444.
- [20] J. Zhang, P. Liu, H. Ma, Y. Ding, Nanostructured porous gold for methanol electro-oxidation, *J. Phys. Chem. C* 111 (2007) 10382–10388.
- [21] C. Xu, J. Su, X. Xu, P. Liu, H. Zhao, F. Tian, Y. Ding, Low temperature CO oxidation over unsupported nanoporous gold, *J. Am. Chem. Soc.* 129 (2007) 42–43.
- [22] R. Roscoe, The plastic deformation of cadmium single-crystals, *Phil. Mag.* 21 (1936) 399–406.
- [23] J.C. Grosskreutz, The effect of oxide films on dislocation - surface interactions in aluminum, *Surf. Sci.* 8 (1967) 173–190.
- [24] M.E. Gurtin, A. Needleman, Boundary conditions in small-deformation, single-crystal plasticity that account for the burgers vector, *J. Mech. Phys. Solids* 53 (1) (2005) 1–31.
- [25] M. Ekh, S. Bargmann, M. Grymer, Influence of grain boundary conditions on modeling of size-dependence in polycrystals, *Acta Mech.* 218 (1–2) (2011) 103–113.
- [26] I. Özdemir, Yalçinkaya, Modeling of dislocation-grain boundary interactions in a strain gradient crystal plasticity framework, *Comput. Mech.* 54 (2) (2014) 255–268.
- [27] P. van Beers, *Multiscale modelling of grain boundary plasticity* (Ph.D. thesis), TU Eindhoven, Netherlands, 2015.
- [28] D. Gottschalk, A. McBride, B.D. Reddy, A. Javili, P. Wriggers, Computational and theoretical aspects of a grain-boundary model that accounts for grain misorientation and grain-boundary orientation, *Comput. Mater. Sci.* 111 (2016) 443–459.
- [29] E. Bayerschen, A. McBride, B. Reddy, T. Böhlke, Review on slip transmission criteria in experiments and crystal plasticity models, *J. Mater. Sci.* 51 (5) (2016) 2243–2258.
- [30] D.E. Hurtado, M. Ortiz, Surface effects and the size-dependent hardening and strengthening of nickel micropillars, *J. Mech. Phys. Solids* 60 (8) (2012) 1432–1446.
- [31] X.L. Peng, G.Y. Huang, Modeling dislocation absorption by surfaces within the framework of strain gradient crystal plasticity, *Internat. J. Solids Structures* 72 (2015) 98–107.
- [32] S. Bargmann, B. Svendsen, M. Ekh, An extended crystal plasticity model for latent hardening in polycrystals, *Comput. Mech.* 48 (6) (2011) 631–645.
- [33] M. Ekh, M. Grymer, K. Runesson, T. Svedberg, Gradient crystal plasticity as part of the computational modelling of polycrystals, *Internat. J. Numer. Methods Engrg.* 72 (2) (2007) 197–220.
- [34] M. Kuroda, V. Tvergaard, On the formulations of higher-order strain gradient crystal plasticity models, *J. Mech. Phys. Solids* 56 (8) (2008) 1591–1608.
- [35] R.M. Keller, S.P. Baker, E. Arzt, Effects of film thickness, grain size, and passivation, *J. Mater. Res.* 13 (5) (1998) 1307–1317.
- [36] C. Zhou, S. Biner, R. LeSar, Simulations of the effect of surface coatings on plasticity at small scales, *Acta Mater.* 63 (11) (2010) 1096–1099.
- [37] A.T. Jennings, C. Gross, F. Greer, Z.H. Aitken, S.W. Lee, C.R. Weinberger, J.R. Greer, Higher compressive strengths and the Bauschinger effect in conformally passivated copper nanopillars, *Acta Mater.* 60 (8) (2012) 3444–3455.
- [38] D. Kiener, C. Motz, M. Rester, M. Jenko, G. Dehm, FIB damage of Cu and possible consequences for miniaturized mechanical tests, *Mater. Sci. Eng. A* 459 (1) (2007) 262–272.
- [39] J. Mayer, L.A. Giannuzzi, T. Kamino, J. Michael, TEM sample preparation and FIB-induced damage, *MRS Bull.* 32 (5) (2007) 400–407.
- [40] J. Hütsch, E.T. Lilleodden, The influence of focused-ion beam preparation technique on microcompression investigations: Lathe vs. annular milling, *Scr. Mater.* 77 (2014) 49–51.
- [41] J.J. Gilman, Oxide surface films on metal crystals, *Science* 306 (5699) (2004) 1134–1135.
- [42] S.H. Oh, C. Rentenberger, J. Im, C. Motz, D. Kiener, H.P. Karnthaler, G. Dehm, Dislocation plasticity of Al film on polyimide investigated by cross-sectional in situ transmission electron microscopy straining, *Scr. Mater.* 65 (5) (2011) 456–459.
- [43] M. Wohlgenuth, N. Yufa, J. Hoffman, E.L. Thomas, Triply periodic bicontinuous cubic microdomain morphologies by symmetries, *Macromolecules* 34 (17) (2001) 6083–6089.
- [44] M. Ziehmer, K. Hu, K. Wang, E.T. Lilleodden, A principle curvatures analysis of the isothermal evolution of nanoporous gold: Quantifying the characteristic length-scales, *Acta Mater.* 120 (2016) 24–31.
- [45] S. Bargmann, C. Soyarslan, E. Husser, N. Konchakova, Computational modeling of the mechanical behavior of gold-polymer nanocomposites, *Mater. Based Des. Struct.* 94 (2016) 53–65.